Check for updates

A "belt" strategy for promoting the 3D network packing of fully non-fused ring acceptors in organic solar cells†

Tianqiang Cui,‡[a] Zhan Huang,‡[a] Yamin Zhang, [ID] *[a] Xiao-Peng Ru,[a] Xingqi Bi,[b] Yun-Tao Ding,[a] Yongrui Yang,[cd] Junpeng Dai,[e] Guanghao Lu,[e] Zitong Liu,[a] Yongsheng Chen [ID] *[b] and Hao-Li Zhang [ID] *[a]

Fully non-fused ring acceptor (NFRA) materials have higher structural diversity than their fused ring counterparts, which have the potential to further promote the performance of organic solar cells and reduce the materials cost. However, owing to their non-fused structural nature, it is difficult for NFRAs to achieve the desirable fully planar state during film formation, which ultimately impedes the device performance. To date, the lack of efficient control over the molecular conformation in both solution and solid states remains a major challenge in the material design of NFRAs. Here, we propose a novel "belt" strategy for construction of a high performance NFRA, which is based on installing a bulky cyclic side chain for more efficient tailoring of the molecular conformation. The molecule with a cyclic "belt" (CSO4TIC) shows a more desirable 3D network packing structure and conformation stability as compared with the molecule with conventional linear side chains (LSO4TIC). Notably, the device based on CSO4TIC achieved a power conversion efficiency of 14.22%, placing it among the top efficiencies reported to date for NFRAs. It is believed that this is the pioneering instance of incorporating a cyclic "belt" into NFRA materials, providing a new route towards low cost and high performance organic photovoltaic materials design.

Introduction

Organic solar cells (OSCs), based on organic semiconducting materials, have broad application prospects in lightweight near-space vehicles, building-integrated photovoltaics, wearable devices, and smart greenhouses, among other fields. In the past two decades, the field of OSCs has experienced rapid development. Currently, the power conversion efficiency (PCE) of single-junction organic photovoltaic devices has exceeded 19%,[1–5] while for tandem devices, the PCE has exceeded 20%.[6] The improvement in efficiency of organic photovoltaics relies mainly on the design innovation of active layer materials, with the development of new electron acceptor materials being an important part of this process.

Since the introduction of an A-D-A type non-fullerene fused-ring electron acceptor (FREA) by Zhan *et al.* in 2015,[7] small molecule electron acceptors have garnered significant attention. Currently, derivatives of the A-D-A′-D-A-type fused-ring electron acceptor Y6,[8] developed by Zou *et al.*, have achieved an efficiency of approximately 19%. While FREAs have shown excellent performance in photovoltaic conversion, their construction usually requires multiple synthesis steps. Compared to FREAs, non-fused ring acceptors (NFRAs) have a more diverse set of molecular building blocks and more flexible connection methods.[9–20] For the structural design of NFRAs, it is necessary to draw on the experience gained from the design of FREAs. Through analysis of high-performance FREAs, we could discern the factors contributing to their high PCE and draw valuable insights. Key aspects that can be gleaned include: (1) employing a highly planar backbone; (2) incorporating end groups with strong electron-withdrawing ability and pronounced stacking capability; (3) ensuring an appropriate dihedral angle between the side chains and the backbone to

[a]*State Key Laboratory of Applied Organic Chemistry (SKLAOC), Key Laboratory of Special Function Materials and Structure Design (MOE), College of Chemistry and Chemical Engineering, Lanzhou University, Lanzhou 730000, China. E-mail: haoli. zhang@lzu.edu.cn; zym@lzu.edu.cn*

[b]*State Key Laboratory and Institute of Elemento-Organic Chemistry, The Centre of Nanoscale Science and Technology, Key Laboratory of Functional Polymer Materials, Renewable Energy Conversion and Storage Center (RECAST), College of Chemistry, Nankai University, Tianjin 300071, China. E-mail: yschen99@nankai.edu.cn*

[c]*CAS Key Laboratory of Green Printing, Beijing National Laboratory for Molecular Science (BNLMS), Institute of Chemistry, Chinese Academy of Sciences, Beijing, 100190, China*

[d]*University of Chinese Academy of Sciences, Beijing 100049, China*

[e]*Frontier Institute of Science and Technology, Xi'an Jiaotong University, Xi'an 710054, China*

† Electronic supplementary information (ESI) available. CCDC 2277927 and 2277928. For ESI and crystallographic data in CIF or other electronic format see DOI: https://doi.org/10.1039/d3ta07296g

‡ These authors contributed equally to this work.

6996 | *J. Mater. Chem. A*, 2024, **12**, 6996–7004

This journal is © The Royal Society of Chemistry 2024

guarantee molecular solubility and favorable stacking mode; (4) exhibiting a 3D network packing structure that is more conducive to promoting charge transfer.[21–23]

Achieving the advantages of efficient FREAs in synchrony presents a significant challenge for NFRAs. The most critical issue is developing a strategy to guarantee the planarity of NFRAs' molecular backbone. To ensure the planarity of the molecular backbone, the current approach mainly relies on non-covalent intramolecular interactions (NIIs) (including O···S, S···N, S···F, etc.)[24] to lock the conformation of the individual units in NFRAs. However, in the solution state, it is difficult to lock the molecular conformation with NIIs, resulting in various intermediate conformations during the film formation process from the solution state. This leads to difficulties in achieving a fully planar state of the acceptor molecules, which in turn hinders the breakthrough of device efficiency. Given that NIIs often require the assistance of steric hindrance in locking molecular conformations,[25] it is believed that steric hindrance could certainly serve as a potential conformation-locking mechanism solely. Besides, the incorporation of alkyl side-chains is crucial in altering the charge transport properties of organic semiconductors in the solid state, by fine-tuning the intermolecular interactions and the molecular packing pattern. Recent studies have demonstrated that aromatic side chains with high steric hindrance (such as bis(4-butylphenyl) amino reported by Bo et al.,[26] triisopropyl phenyl reported by Hou et al.[27] and chlorinated diaryl amino reported by Li et al.[28]) can lead to more desirable molecular packing with improved device performance.

Here, we propose a novel "belt" strategy for construction of a high performance NFRA, which is based on installing a bulky cyclic side chain (the "belt") in the middle of the molecule. A fully non-fused ring acceptor containing a cyclic "belt", named CSO4TIC, was designed and synthesized. For comparison, its counterpart, named LSO4TIC, with linear alkyl chains was also synthesized. We demonstrate that such a simple cyclic "belt" can provide efficient steric hindrance between the central units, which tailors the torsion angle between constituent units while ensuring good solubility and a favorable 3D network molecular packing structure of NFRA materials. After systematically comparing the differences between CSO4TIC and LSO4TIC in molecular conformation, packing structure and photovoltaic performance, it is believed that such a "belt" strategy opens a new route for efficient molecular conformation control, promotes the formation of 3D network packing structures, and enhances the corresponding device photovoltaic performance.

Results and discussion

Molecular design

To reduce the conformational disorder of fully non-fused ring acceptor molecules in the solution state and achieve ideal skeleton planarity in the thin-film state, a rigid cyclic side chain was introduced to control the planarity of the molecular structure and provide spatial steric hindrance that facilitates the formation of 3D network packing of the acceptors. Based on this idea, the acceptor molecule CSO4TIC (Fig. 1a) was designed and synthesized. As shown in the single-crystal structure in Fig. 1b, the torsion angle between the two thiophenes connected with the cyclic side chain is 0° and the dihedral angle between the cyclic side chain and the thiophenes is 76.79°, demonstrating that this cyclic side chain can effectively fix the conformation of the backbone and provide an appropriate steric hindrance to avoid excessive molecular aggregation.

Meanwhile, acceptor LSO4TIC (Fig. 1a) with the same elemental composition but a linear side chain was also
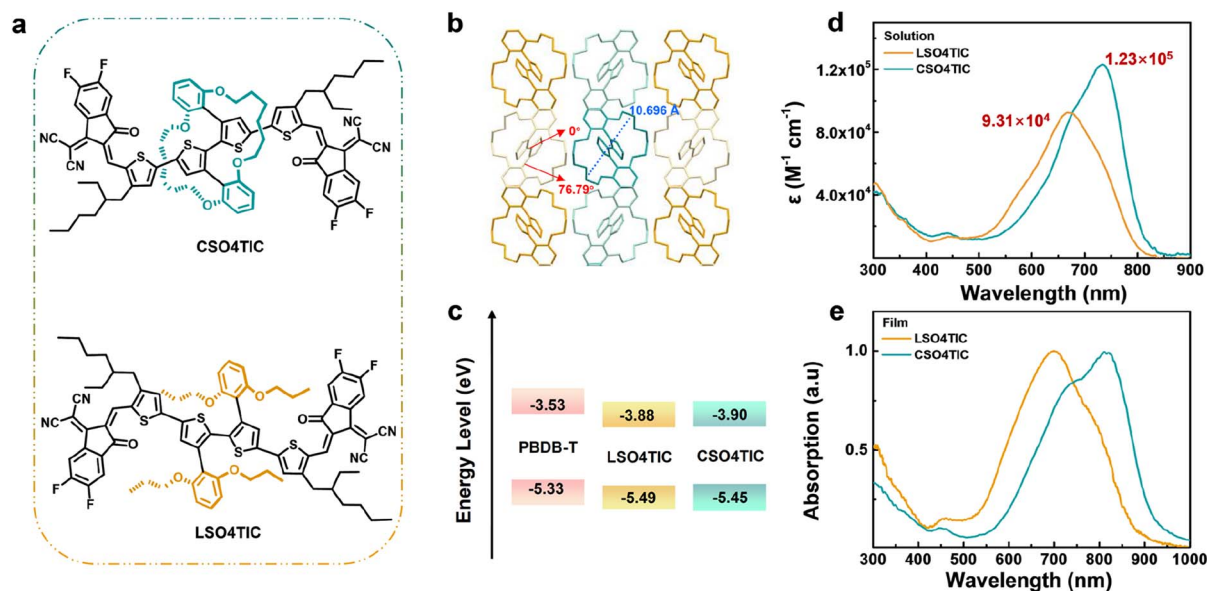

Fig. 1 (a) Molecular structures of CSO4TIC and LSO4TIC; (b) single-crystal structure of bithiophenes connected with the cyclic side chain; (c) energy level diagram of the donor material PBDB-T, acceptor material LSO4TIC and acceptor material CSO4TIC; The UV-Vis absorption spectra of CSO4TIC and LSO4TIC in (d) chloroform and (e) film state.

This journal is © The Royal Society of Chemistry 2024

J. Mater. Chem. A, 2024, **12**, 6996–7004 | **6997**

Table 1 Optical, thermal, and electrochemical analysis data of LSO4TIC and CSO4TIC

Materials	λ_{max}^{sol} [nm]	λ_{max}^{film} [nm]	λ_{edge}^{film} [nm]	ε [M^{-1} cm^{-1}]	E_g^{opt} [eV]	HOMO [eV]	LUMO [eV]	T_d [°C]
CSO4TIC	734	816	912	1.23×10^5	1.36	−5.45	−3.90	340.3
LSO4TIC	666	700	872	9.31×10^4	1.42	−5.49	−3.88	316.0

synthesized, aiming to illustrate the different roles of the cyclic-type and the linear side chains in fully non-fused ring acceptors. The detailed synthetic procedures are described in the "Materials and Synthesis" section of the ESI.†

Photophysical and electrochemical properties

Electrochemical cyclic voltammetry (CV) was used to measure the frontier orbital energy levels of these two acceptor materials, as shown in Fig. S1a† and 1c. The lowest unoccupied molecular orbital (LUMO) energy levels of LSO4TIC and CSO4TIC were −3.88 and −3.90 eV, respectively, while their highest occupied molecular orbital (HOMO) energy levels were −5.49 and −5.45 eV. Compared with LSO4TIC, CSO4TIC showed slightly higher frontier orbital energy levels and a narrower bandgap. This could be attributed to the rigidity of the cyclic side chain, which causes the oxygen atoms located on it to have a more fixed and closer position to the molecular backbone, strengthening the conjugative effect between oxygen atoms and the molecular backbone and enabling more efficient electron delocalization. The UV-Vis absorption spectra of these two NFRAs in solution and thin films are shown in Fig. 1d and e. In dilute chloroform solution, the molar extinction coefficients (ε) of CSO4TIC and LSO4TIC at 734 and 666 nm were 1.23×10^5 and 9.31×10^4 M^{-1} cm^{-1}, respectively. The higher molar absorption coefficient of CSO4TIC may originate from its higher planar conformation in the solution state. In pure thin films, the absorption spectra of both materials experienced a redshift. For LSO4TIC, the maximum absorption peak and cutoff absorption edge were located at 700 nm and 872 nm, respectively, with an optical bandgap (E_g^{opt}) of 1.42 eV. For CSO4TIC, the film absorption peak appeared at 816 nm and the cutoff absorption edge was around 912 nm, corresponding to an E_g^{opt} of 1.36 eV (the detailed parameters are summarized in Table 1). As shown in Fig. S1c and d,† the photoluminescence quantum yields (PLQYs) of LSO4TIC and CSO4TIC in the solution state are 10.17% and 13.33%, respectively, while in the thin film state, the PLQYs of LSO4TIC and CSO4TIC are 8.97% and 6.84%, respectively. Thermogravimetric analysis (TGA) curves measured the decomposition temperatures of LSO4TIC and CSO4TIC at 5% weight loss to be 316.0 °C and 340.3 °C, respectively (Fig. S1b†). The higher decomposition temperature of CSO4TIC ensures the thermal stability of OSC devices based on it under continuous light irradiation.

Stabilities of molecular conformation and packing states

Due to the increase in temperature, the interaction between molecules and the solvation effect between molecular chains are weakened, leading to accelerated molecular thermal motion. Therefore, temperature-dependent nuclear magnetic resonance (NMR) experiments are one of the important methods for conformational analysis. The temperature-dependent ^{1}H NMR technique was used to test the compounds CSO4TIC and LSO4TIC at different temperatures. When the temperature increased from 25 °C to 100 °C, the chemical shifts of the protons on the side chain phenyl ring of CSO4TIC (in tetrachloroethane-d$_2$) moved gradually from their respective positions to low fields by 0.021 ppm (H$_e$) and 0.047 ppm (H$_d$) (Fig. 2a). For LSO4TIC (in tetrachloroethane-d$_2$), H$_e$ and H$_d$ moved to low fields by 0.152 ppm and 0.187 ppm, respectively (Fig. 2b). Additionally, with increasing temperature, the chemical shift of the thiophene proton (H$_c$) in CSO4TIC gradually moved from 6.845 ppm to 6.933 ppm, while the chemical shift of H$_c$ in LSO4TIC did not change. This information suggests that during the heating process, the cyclic side chain of CSO4TIC only experienced a certain amount of twisting, while the linear side chain of LSO4TIC experienced significant swinging. In addition, owing to the rigidity of the cyclic side chain, it exhibits distinct magnetic and electrical properties in different directions, resulting in the splitting of the H$_f$ resonance peak on the side chain into two peaks (4.062 ppm and 3.659 ppm). While the flexible linear side chain of LSO4TIC possesses isotropy, H$_f$ in LSO4TIC only shows one chemical shift value, and the chemical shift change of this H$_f$ during the temperature elevation is greater. We prepared pure films of CSO4TIC and LSO4TIC and tested the absorption changes of these films during continuous thermal annealing at 80 °C to explore the stability of their packing state. From the UV-Vis absorption spectra in Fig. 2c and d and the relative absorption intensities of the 0–0 and 0–1 vibronic transitions, *i.e.*, I^{0-0}/I^{0-1} values, in Fig. 2e and f, it can be seen that the packing state of CSO4TIC barely changes during the annealing process, while the shoulder peak of LSO4TIC will gradually strengthen with increasing annealing time. This suggests that the conformation of CSO4TIC molecules can be perfectly inherited from solution to the film state, without causing differences in conformation after film formation due to changes in processing conditions, while the packing mode of LSO4TIC is more easily affected by preparation conditions.

Single-crystal

The single-crystal data can be used to confirm the molecular geometric structure and intermolecular stacking patterns and then establish a correlation between the molecular structure and its charge transport properties. We obtained the single crystals of LSO4TIC and CSO4TIC by the vapor diffusion method. As shown in Fig. 3a, for the single molecular configuration of CSO4TIC, the dihedral angles between the cyclic side chain and the backbone are 77.60° and 76.34°, respectively. The
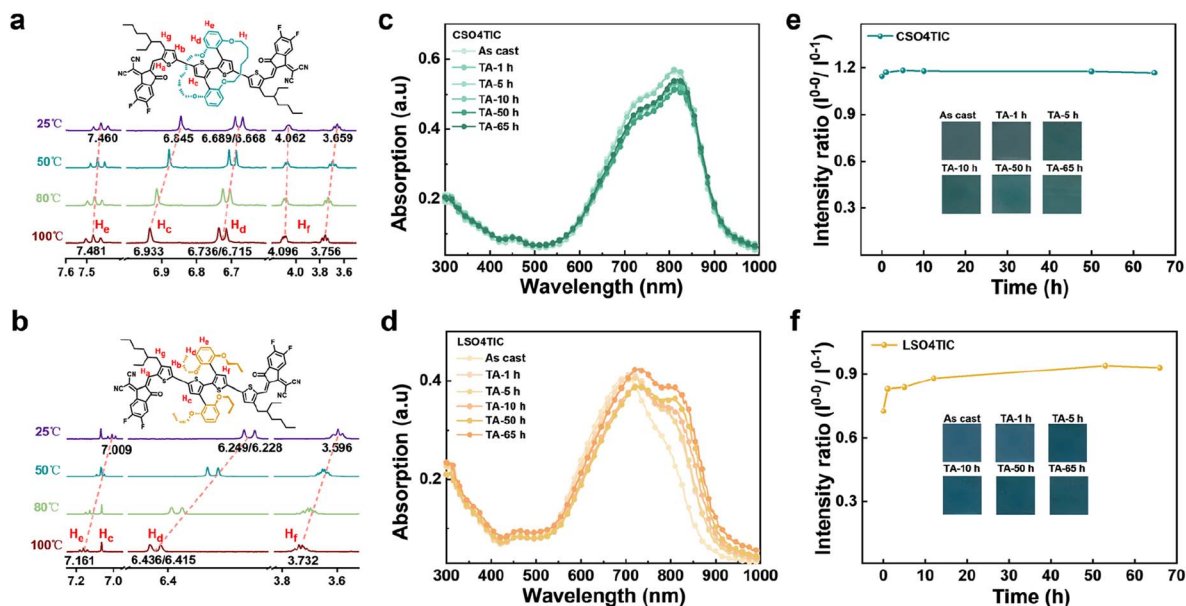
6998 | *J. Mater. Chem. A*, 2024, **12**, 6996–7004

This journal is © The Royal Society of Chemistry 2024

Fig. 2 (a and b) Temperature-dependent ^1H NMR spectra of CSO4TIC and LSO4TIC in tetrachloroethane-d_2 at 400 MHz; (c and d) the absorption changes of CSO4TIC and LSO4TIC pure films during continuous thermal annealing at 80 °C; (e and f) the change in I^{0-0}/I^{0-1} values and film colors under continuous thermal annealing at 80 °C.
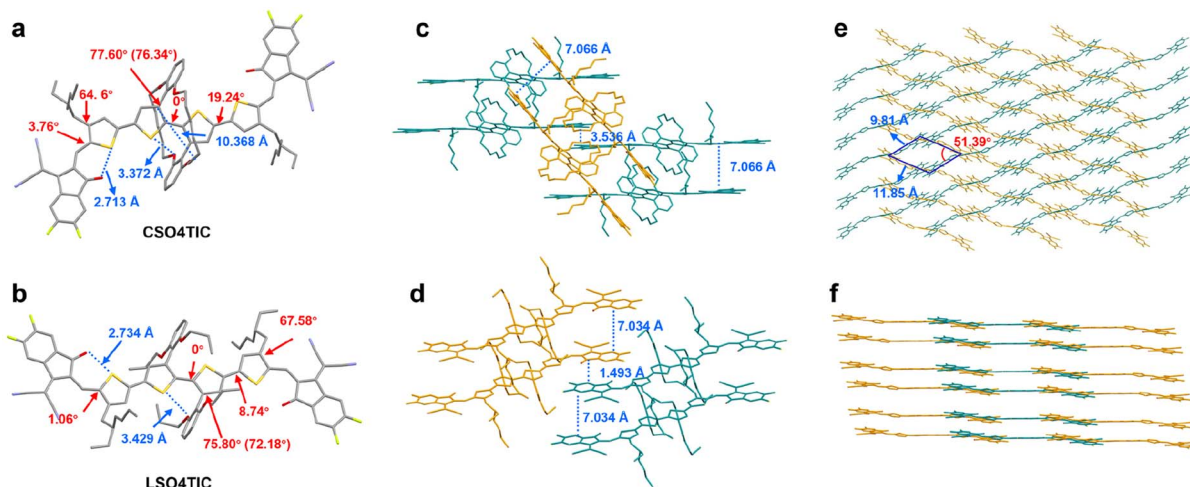

Fig. 3 (a and b) Single-crystal structures of CSO4TIC and LSO4TIC; (c and d) molecular packing of CSO4TIC and LSO4TIC molecules from views along the π-plane; (e) the 3D network packing structure of CSO4TIC; (f) the lamellar packing structure of LSO4TIC.

dihedral angles between the two thiophenes in the core are 0°, and the dihedral angles between the two thiophenes in the core and their adjacent thiophenes are 19.24°. Moreover, relaxed potential surface energy scans were also performed. Fig. S2a and c† show the energy-torsion angle curves of the two central thiophenes in CSO4TIC and LSO4TIC molecules. It can be seen that the rotamer with the two thiophenes adopting an opposite position is the lowest energy conformation of these molecules, which is in agreement with the information obtained from the single crystal data. The distance between the oxygen (O) atoms on the cyclic side chain and the sulfur (S) atoms on the backbone is 3.372 Å, which is greater than the sum of the van der Waals radii of the O and S atoms (3.32 Å),[29] so it can be

considered that there is no non-covalent interaction between the O and S atoms in CSO4TIC, and its planarity is completely realized by the large cyclic-type bulky group. From the single molecular configuration of LSO4TIC (Fig. 3b), the dihedral angles between the linear side chain and the backbone are 75.80° and 72.18°, respectively. The dihedral angles between the two central thiophenes are also 0°, and the dihedral angles between the two central thiophenes and their adjacent thiophenes are 8.74°, showing higher planarity than CSO4TIC. The distance between the O atoms on the linear side chain and the S atoms on the backbone is 3.429 Å, which is also greater than the sum of the van der Waals radii of the O and S atoms. As can be seen from Fig. 3c–f, S3 and S4,† although it's just a difference

between whether the side chain is ring-shaped or not, the packing states of LSO4TIC and CSO4TIC are completely different. For CSO4TIC, two molecules are packed into a pair and the distance between two molecules is 7.066 Å, while the π–π stacking distance between a pair of molecules and another pair of molecules parallel to each other is 3.536 Å. Due to the steric hindrance of the cyclic side chain, the molecules will be interlaced with each other at an angle of 51.39°, forming a 3D network packing structure, and the void size of the CSO4TIC molecules is smaller than that of the Y series molecules,[30] which suggests CSO4TIC's superior charge transport ability. It is worth emphasizing that CSO4TIC is one of the few non-fused ring acceptor molecules that could form a 3D network packing structure (Table S1†). Unlike CSO4TIC, the flexibility of the linear side chains in LSO4TIC makes it difficult for each pair of LSO4TIC molecules to form well-ordered π–π stacking and a 3D network packing structure, resulting in lamellar stacking with a large interlayer spacing (7.034 Å).

At the same time, the surface electrostatic potential, transfer integral, reorganization energy and mobility of the two molecules are also calculated based on the single crystal data. It can be seen from Fig. S5† that the surface electrostatic potentials of CSO4TIC and LSO4TIC are very similar, and the dipole moments of both are 0 debye due to high structural symmetry. The magnitude of reorganization energy is inversely proportional to the charge transport capacity, and the hole reorganization energy of CSO4TIC and LSO4TIC is greater than their electron reorganization energy (Table S2†), indicating that they are both prone to show electron transport behaviors. As shown in Fig. S6,† the charge-transfer integrals for electron transport of CSO4TIC are greater than its charge-transfer integrals for hole transport. According to Marcus charge transfer theory, the hole and electron transport rate constants of the system can be calculated from the reorganization energy and transfer integral, which could then be used to determine the hole and electron mobility of the molecules. As listed in Table S3,† CSO4TIC has a stronger electron transport tendency with higher electron mobility compared to LSO4TIC.

Photovoltaic performance

To study the impact of cyclic-type and linear side chains on photovoltaic performance, a conventional device structure with the composition of indium tin oxide (ITO)/poly(3,4-ethyl-enedioxythiophene):poly(styrene-sulfonate) (PEDOT:PSS)/PBDB-T/CSO4TIC (LSO4TIC)/3,3′-(1,3,8,10-tetraoxanthra[2,1,9-def:6,5,10-d′e′f′] diisoquinoline-2,9(1H, 3H, 8H, 10H)-diyl) bis(N,N-dimethylpropan-1-amine oxide) (PDINO)/Ag was used to fabricate organic solar cells. It needs to be emphasized that, compared with the blend casting (BC) method, the active layer prepared by the sequential casting (SC) method could achieve higher PCEs in these devices, so the SC method was adopted to systematically optimize the organic photovoltaic devices based on LSO4TIC and CSO4TIC. The optimal device current density–voltage (J–V) characteristics are shown in Fig. 4a, and the specific parameters and optimization procedures of the device are detailed in Tables 2 and S5–S13.† The optimal device based
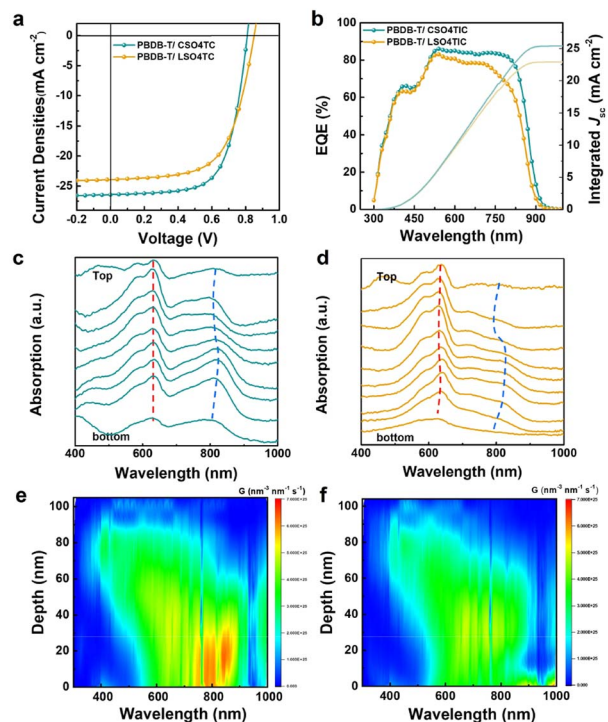

Fig. 4 (a) The J–V and (b) EQE curves of the devices based on PBDB-T/CSO4TIC and PBDB-T/LSO4TIC; (c and d) film-depth-dependent light absorption spectra and (e and f) exciton generation contours of the PBDB-T/CSO4TIC and PBDB-T/LSO4TIC films cast by the SC method.

on LSO4TIC has an open-circuit voltage (V_{oc}) of 0.857 V, a short-circuit current density (J_{sc}) of 23.43 mA cm^{-2}, and a fill factor (FF) of 63.38%, resulting in a PCE of 12.72%. While the device based on CSO4TIC achieves a high J_{sc} of 26.00 mA cm^{-2} and a FF of 67.52%, demonstrating a higher PCE of 14.22%. Moreover, the external quantum efficiency (EQE) of devices based on LSO4TIC and CSO4TIC shows a wide range of light responses from 300 to 900 nm (Fig. 4b). The integral current density values of the EQE spectra of devices based on LSO4TIC and CSO4TIC are 22.89 and 25.42 mA cm^{-2}, respectively, which are very consistent with the values determined from the J–V curves within a 5% mismatch range.

Furthermore, we analyzed the exciton dissociation and charge collection characteristics of the devices based on PBDB-T/LSO4TIC and PBDB-T/CSO4TIC. The curve of photocurrent density (J_{ph}) versus effective voltage (V_{eff}) was used to evaluate the charge separation and extraction probability in the solar cells. From Fig. S7a,† it is observed that the J_{ph} increases with an increase in V_{eff}, and all the J_{ph} values can reach saturation (J_{sat}) when V_{eff} reaches approximately 2 V. To evaluate the probability of charge separation at the donor/acceptor interface, the ratio of J_{ph}/J_{sat} was calculated.[31] The free charge separation and extraction efficiencies of the CSO4TIC-based device estimated from J_{ph}/J_{sat} are higher than those of the LSO4TIC-based device under the short circuit conditions (96.11% and 95.46% for CSO4TIC and LSO4TIC, respectively). This indicates that the CSO4TIC-based device has higher exciton dissociation and charge

7000 | J. Mater. Chem. A, 2024, 12, 6996–7004

This journal is © The Royal Society of Chemistry 2024

Table 2 Photovoltaic parameters of the PBDB-T/CSO4TIC and PBDB-T/LSO4TIC-based devices

Active layers	V_{oc} [V]	J_{sc} [mA cm^{-2}]	J_{sc}^{cala} [mA cm^{-2}]	FF [%]	PCE$_{max}$ [%]
PBDB-T/CSO4TIC	0.810 (0.809 ± 0.002)	26.00 (25.95 ± 0.28)	25.42	67.52 (66.48 ± 0.70)	14.22 (13.95 ± 0.13)
PBDB-T/LSO4TIC	0.857 (0.848 ± 0.006)	23.43 (23.64 ± 0.23)	22.89	63.38 (62.55 ± 0.48)	12.72 (12.53 ± 0.16)

[a] J_{sc}^{cal} is integrated from EQE curves.

collection efficiencies thus leading to higher J_{sc} and FF. Additionally, the J_{ph}-light intensity (P) relationship is measured to understand charge recombination in these devices. Their relationship can be described by the formula $J_{ph} \propto P^{\alpha}$, with $\alpha = 1$ if there is no bimolecular recombination.[32] As shown in Fig. S7b,† the α values for CSO4TIC and LSO4TIC-based devices are 0.911 and 0.909, respectively. All values are close to 1, implying that little bimolecular recombination occurred in these devices. In the absence of light, the electrochemical impedance spectrum in Fig. S7c† was tested at a frequency of 0.01–100 kHz.[33] The resistance value of the device based on LSO4TIC is greater than that based on CSO4TIC, indicating that the device based on CSO4TIC has fewer interface defects, thus further inhibiting charge recombination.

Suppressing energy loss (E_{loss}) through rational molecular design is an important approach to improving the efficiency of organic photovoltaic devices. In general, the E_{loss} can be quantified using three components from the equation below:

$$E_{loss} = q\Delta V_{loss} = E_g - qV_{oc} = (E_g - qV_{oc}^{sq}) + (qV_{oc}^{sq} - qV_{oc}^{rad}) + (qV_{oc}^{rad} - qV_{oc}) = \Delta E_1 + \Delta E_2 + \Delta E_3$$

Among them, V_{oc}^{sq} is the maximum voltage under the Shockley–Queisser (SQ) limit and V_{oc}^{rad} is the open-circuit voltage when only radiative recombination exists in the device. ΔE_1 is the energy difference between E_g and V_{oc} in the SQ limit ($E_g - qV_{oc}^{sq}$), and this loss is caused by radiative recombination above the bandgap, which is inevitable for any type of solar cell.[34] The bandgap E_g is estimated by Fourier-transform photocurrent spectroscopy external quantum efficiency (FTPS-EQE), as shown in Fig. S8a,† and the E_gs of CSO4TIC and LSO4TIC-based blended films are estimated to be 1.422 and 1.448 eV, respectively (Fig. S8c and d, Table S14†). Therefore, the ΔE_1 of OSCs based on CSO4TIC and LSO4TIC could be calculated to be 0.263 and 0.265 eV, respectively. The ΔE_2 values of CSO4TIC and LSO4TIC-based devices are estimated to be 0.058 and 0.069 eV, respectively. The lower ΔE_2 is related to the more ordered molecular packing of CSO4TIC. The ΔE_3 of OSCs based on CSO4TIC and LSO4TIC are 0.300 and 0.269 eV, respectively, which is because V_{oc}^{sq} is related to the bandgap ($V_{oc}^{sq} = 0.941E_g - 0.171$).[35] The non-radiative recombination loss ($\Delta E^{non-rad}$) of the devices can be calculated from the external quantum efficiency of electroluminescence (EQE$_{EL}$) ($\Delta E^{non-rad} = -kT\ln(EQE_{EL})$) (Fig. S8b†), and the $\Delta E^{non-rad}$ values of CSO4TIC and LSO4TIC are calculated to be 0.249 and 0.253 eV, respectively, which are relatively low in fully non-fused acceptors.

Film-depth-dependent light absorption spectroscopy (FLAS) was used to characterize the vertical distribution of donor and acceptor components in the active layer obtained by sequential deposition and post-treatment, to further understand the charge generation, transport, and collection processes in the corresponding devices.[36] As shown in Fig. 4c and d, the absorption peaks at around 628 nm are contributed by the donor material PBDB-T (see Fig. S9a† for the absorption spectrum of a pure PBDB-T film), and the absorption peak at around 816 nm in Fig. 4c is contributed by CSO4TIC, while the absorption peak at around 810–825 nm in Fig. 4d is contributed by LSO4TIC. The different absorption features of donors and acceptors allow us to quantify the material composition in the active layer. We define the side of the device where light enters as the bottom, and it can be seen that for the active layer composed of PBDB-T and CSO4TIC, the acceptor levels are relatively uniform along the vertical direction from the bottom to the top of the active layer. In the LSO4TIC-based system, however, the acceptor levels vary significantly along the vertical direction, indicating that the charge transport levels have fluctuations along the vertical direction of the film, which is unfavorable for obtaining a high fill factor. At the same time, based on the extinction coefficient (k) obtained by FLAS and the refractive index (n) measured by other methods, the exciton generation process in the device can be simulated and calculated using the optical interference transfer matrix model. As can be seen from Fig. 4e and f, for the PBDB-T/CSO4TIC and PBDB-T/LSO4TIC systems, a large number of excitons are generated close to the side of the device where light enters (within 50 nm from the bottom of the active layer), while the PBDB-T/CSO4TIC system has a higher exciton generation rate, which is favorable for the corresponding devices to achieve higher J_{sc}. At the same time, considering the location of exciton generation, when they are disassociated into electrons and holes, the electrons need to be transported >50 nm along the acceptor phase to reach the cathode. Therefore, the higher electron mobility of CSO4TIC is beneficial for obtaining higher J_{sc} and FF.

Morphological characteristics

Through wide-angle grazing incidence X-ray scattering (GIWAXS), the intermolecular packing patterns of CSO4TIC and LSO4TIC in neat films and blended films were analyzed. The 2D scattering patterns and in-plane (IP) and out-of-plane (OOP) scattering profiles are shown in Fig. 5a–f. For CSO4TIC pure films, (010) diffraction signals can be resolved at 1.73 Å^{-1} in both OOP and IP directions, corresponding to a compact π–π stacking distance of 3.63 Å. However, the higher peak intensity in the OOP direction indicates that CSO4TIC exhibits a more preferential face-on molecular packing. The peak at 0.43 Å^{-1} in

This journal is © The Royal Society of Chemistry 2024

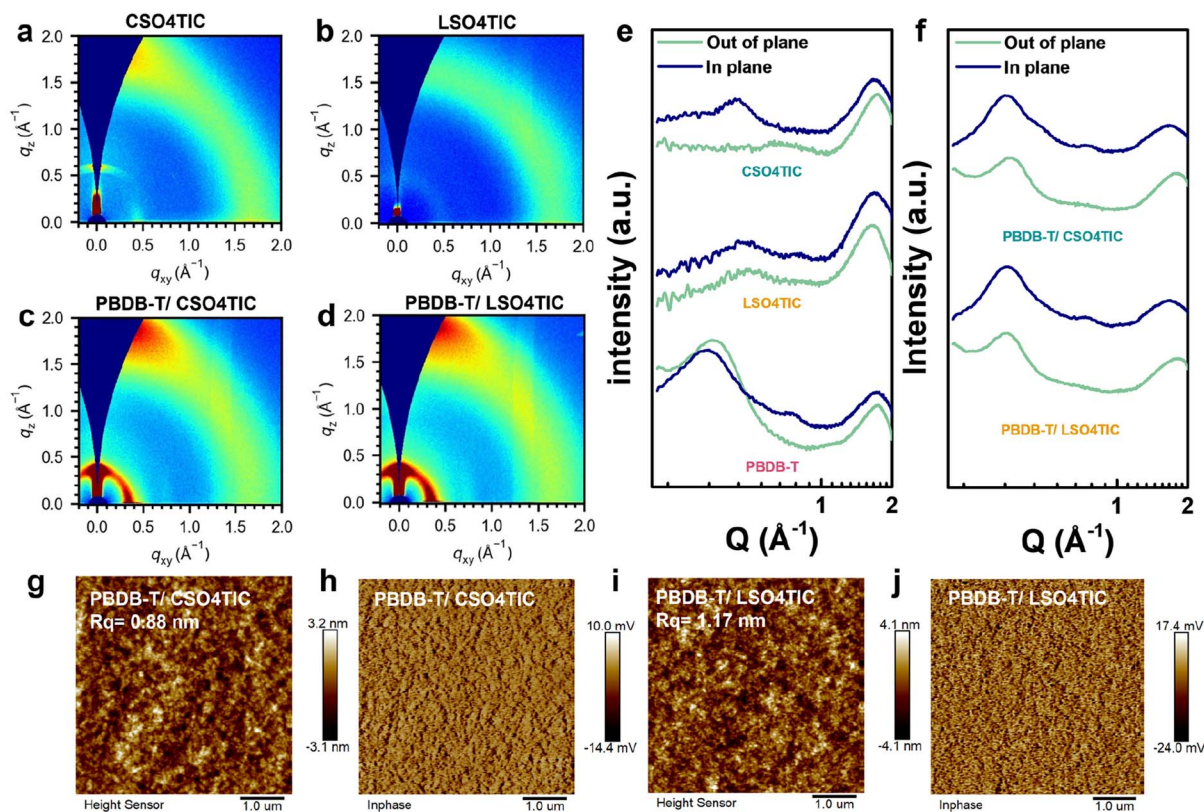*J. Mater. Chem. A*, 2024, **12**, 6996–7004 | **7001**

Fig. 5 (a–d) GIWAXS patterns of the neat and blend films of CSO4TIC and LSO4TIC; (e and f) the IP and OOP extracted line−cut profiles of the neat and blend films of CSO4TIC and LSO4TIC; AFM (g and i) height images and (h and j) phase images of PBDB-T/CSO4TIC and PBDB-T/LSO4TIC.

the IP direction is attributed to a lamellar stacking distance of 14.60 Å. For LSO4TIC neat films, 1.64 Å^{-1} (010) and 0.48 Å^{-1} (100) diffraction peaks can be observed in both OOP and IP directions, corresponding to 3.83 Å π–π stacking distance and 13.08 Å lamellar stacking distance. The molecular packing properties obtained by GIWAXS are different from those obtained by single crystals to some extent, because polymorph and orientation distribution increase the complexity of the molecular packing structure in the GIWAXS-measured thin films.[37] In the PBDB-T/CSO4TIC and PBDB-T/LSO4TIC blend films obtained by sequential deposition, their (010) peaks are broadened to a higher q region than those of the neat donor and acceptor films, indicating that the π–π stacking distance of the blend films is smaller (3.52 Å for PBDB-T/CSO4TIC and 3.57 Å for PBDB-T/LSO4TIC), showing enhanced crystalline features. This may be due to the solid additives DBCl (1,3-dibromo-5-chlorobenzene) and 2-IN (2-iodonaphthalene) effectively improving the molecular packing in PBDB-T/CSO4TIC and PBDB-T/LSO4TIC blend films, respectively, and the enhanced molecular interaction is beneficial for charge transport in OPV devices. The morphology of PBDB-T/CSO4TIC and PBDB-T/LSO4TIC films was characterized by atomic force microscopy (AFM). As shown in Fig. 5g–i and S10,† for as-cast blended films, the R_q values of PBDB-T/CSO4TIC and PBDB-T/LSO4TIC systems are 0.97 nm and 1.00 nm, respectively. After the addition of solid additives and heat annealing, their R_q values were

0.88 nm and 1.17 nm for PBDB-T/CSO4TIC and PBDB-T/LSO4TIC, respectively. The surfaces of these thin films were very smooth, without any observed large aggregations, regardless of whether post-treatment was performed.

Conclusions

In summary, a fully non-fused ring acceptor, CSO4TIC, based on the "belt" strategy with a bulky cyclic side chain (the "belt"), and its counterpart named LSO4TIC with a linear side chain were designed and synthesized. Although the structures of CSO4TIC and LSO4TIC are very similar, they behaved remarkably differently. Compared with LSO4TIC, CSO4TIC exhibits a higher frontier orbital energy level, narrower bandgap and higher molar absorption coefficient. Meanwhile, CSO4TIC also shows higher thermal stability, packing state stability and conformation stability than LSO4TIC. The planar conformation of the CSO4TIC molecule can be perfectly inherited from the solution state to the film state during the film-forming process, which could be attributed to the efficient conformation control ability of the cyclic side chain. Moreover, from single-crystal XRD, we found that the packing patterns of CSO4TIC and LSO4TIC are completely different. Due to the steric effect of the cyclic side chain, the CSO4TIC molecules are interlaced with each other, forming a 3D network packing structure. However, the flexibility of the linear side chains in LSO4TIC makes it

7002 | J. Mater. Chem. A, 2024, 12, 6996–7004

This journal is © The Royal Society of Chemistry 2024

difficult for LSO4TIC molecules to form well-ordered π–π stacking and a 3D network packing structure, resulting in a lamellar stacking structure with a large interlayer space. When employing PBDB-T as the donor material, the optimal PCE for the OPV device based on CSO4TIC with the sequential casting method reached 14.22%, which is much higher than that of the device based on LSO4TIC (12.72%). It is worth noting that this PCE is among the best efficiencies reported for fully non-fused ring acceptors. These findings suggest that the "belt" strategy holds great promise as a potential approach for future advancements in the field of OSCs.

Author contributions

T. C. and Z. H. contributed equally to this work. Y. Z., Y. C. and H. L. Z. conceived and directed the study. T. C. and X. P. R. synthesized the acceptors. Z. H. fabricated and characterized the photovoltaic devices. X. B. cultivated the single-crystal. Y. T. D. conducted the DFT calculations. Y. Y. collected the GIWAXS data. J. D. and G. L. collected and analyzed the FLAS data. Z. L. participated in the data discussion. The manuscript was mainly prepared by Y. Z. and H. L. Z. All authors participated in the manuscript preparation and commented on the manuscript.

Conflicts of interest

There are no conflicts of interest to declare.

Acknowledgements

Notes and references

1 Y. Cui, Y. Xu, H. Yao, P. Bi, L. Hong, J. Zhang, Y. Zu, T. Zhang, J. Qin, J. Ren, Z. Chen, C. He, X. Hao, Z. Wei and J. Hou, *Adv. Mater.*, 2021, **33**, 2102420.

2 L. Zhan, S. Li, Y. Li, R. Sun, J. Min, Y. Chen, J. Fang, C.-Q. Ma, G. Zhou, H. Zhu, L. Zuo, H. Qiu, S. Yin and H. Chen, *Adv. Energy Mater.*, 2022, **12**, 2201076.

3 J. Fu, P. W. K. Fong, H. Liu, C.-S. Huang, X. Lu, S. Lu, M. Abdelsamie, T. Kodalle, C. M. Sutter-Fella, Y. Yang and G. Li, *Nat. Commun.*, 2023, **14**, 1760.

4 L. Zhu, M. Zhang, J. Xu, C. Li, J. Yan, G. Zhou, W. Zhong, T. Hao, J. Song, X. Xue, Z. Zhou, R. Zeng, H. Zhu,

5 X. Li, A. Tang, H. Wang, Z. Wang, M. Du, Q. Guo, Q. Guo and E. Zhou, *Angew. Chem., Int. Ed.*, 2023, e202306847.

6 Z. Zheng, J. Wang, P. Bi, J. Ren, Y. Wang, Y. Yang, X. Liu, S. Zhang and J. Hou, *Joule*, 2022, **6**, 171–184.

7 Y. Lin, J. Wang, Z. G. Zhang, H. Bai, Y. Li, D. Zhu and X. Zhan, *Adv. Mater.*, 2015, **27**, 1170–1174.

8 J. Yuan, Y. Zhang, L. Zhou, G. Zhang, H.-L. Yip, T.-K. Lau, X. Lu, C. Zhu, H. Peng, P. A. Johnson, M. Leclerc, Y. Cao, J. Ulanski, Y. Li and Y. Zou, *Joule*, 2019, **3**, 1140–1151.

9 X.-B. Gu, J.-H. Gao, Z.-Y. Han, Y.-H. Shi, Y.-N. Wei, Y.-C. Zhang, Q. Peng, Z.-X. Wei, X. Zhang and H. Huang, *Chin. J. Polym. Sci.*, 2023, **41**, 556–563.

10 Z.-P. Yu, Z.-X. Liu, F.-X. Chen, R. Qin, T.-K. Lau, J.-L. Yin, X. Kong, X. Lu, M. Shi, C.-Z. Li and H. Chen, *Nat. Commun.*, 2019, **10**, 2152.

11 Y.-N. Chen, M. Li, Y. Wang, J. Wang, M. Zhang, Y. Zhou, J. Yang, Y. Liu, F. Liu, Z. Tang, Q. Bao and Z. Bo, *Angew. Chem., Int. Ed.*, 2020, **59**, 22714–22720.

12 T. Cui, Y. Zhang, X. Fei, Y.-T. Ding, Z.-Q. Zhang, T. Wang, C.-L. Sun, Q. Zhu, J. Xin, S. Seibt, W. Ma and H.-L. Zhang, *ACS Appl. Energy Mater.*, 2022, **5**, 13861–13870.

13 S. Shen, Y. Mi, Y. Ouyang, Y. Lin, J. Deng, W. Zhang, J. Zhang, Z. Ma, C. Zhang, J. Song and Z. Bo, *Angew. Chem., Int. Ed.*, 2023, **62**, e202316495.

14 Y. Zhou, M. Li, H. Lu, H. Jin, X. Wang, Y. Zhang, S. Shen, Z. Ma, J. Song and Z. Bo, *Adv. Funct. Mater.*, 2021, **31**, 2101742.

15 Q. Yang, R. Wu, L. Yang, W. Liu, X. Meng, W. Zhang, S. Shen, M. Li, Y. Zhou and J. Song, *Dyes Pigm.*, 2024, **221**, 111808.

16 Y. Zhou, P. Liu, S. Shen, M. Li, R. Qin, X. Tang, C. Qin, J. Song, Z. Bo and L. Zhang, *J. Mater. Chem. A*, 2023, **11**, 7498–7504.

17 D. Li, H. Zhang, X. Cui, Y.-N. Chen, N. Wei, G. Ran, H. Lu, S. Chen, W. Zhang, C. Li, Y. Liu, Y. Liu and Z. Bo, *Adv. Mater.*, 2024, **36**, 2310362.

18 X. Wang, R. Zeng, H. Lu, G. Ran, A. Zhang, Y.-N. Chen, Y. Liu, F. Liu, W. Zhang, Z. Tang and Z. Bo, *Chin. J. Chem.*, 2023, **41**, 665–671.

19 X. Zheng, W. Liu, H. Wang, X. Man, G. Ran, X. Yu, H. Lu, Z. Bi, Y. Liu, A. Zhang, W. Ma, X. Xu, Z. Tang, W. Zhang and Z. Bo, *Cell Rep. Phys. Sci.*, 2022, **3**, 101169.

20 H. Lu, W. Liu, G. Ran, J. Li, D. Li, Y. Liu, X. Xu, W. Zhang and Z. Bo, *Adv. Mater.*, 2023, 2307292.

21 Y. Zou, H. Chen, X. Bi, X. Xu, H. Wang, M. Lin, Z. Ma, M. Zhang, C. Li, X. Wan, G. Long, Y. Zhaoyang and Y. Chen, *Energy Environ. Sci.*, 2022, **15**, 3519–3533.

22 S. Dai, J. Zhou, S. Chandrabose, Y. Shi, G. Han, K. Chen, J. Xin, K. Liu, Z. Chen, Z. Xie, W. Ma, Y. Yi, L. Jiang, J. M. Hodgkiss and X. Zhan, *Adv. Mater.*, 2020, **32**, 2000645.

23 L. Ma, S. Zhang and J. Hou, *J. Mater. Chem. A*, 2023, **11**, 481–494.

24 M. Liu, X. Han, H. Chen, Q. Peng and H. Huang, *Nat. Commun.*, 2023, **14**, 2500.

This journal is © The Royal Society of Chemistry 2024

J. Mater. Chem. A, 2024, **12**, 6996–7004 | **7003**

25 N. E. Jackson, B. M. Savoie, K. L. Kohlstedt, M. Olvera de la Cruz, G. C. Schatz, L. X. Chen and M. A. Ratner, *JACS*, 2013, **135**, 10475–10483.

26 X. Wang, H. Lu, Y. Liu, A. Zhang, N. Yu, H. Wang, S. Li, Y. Zhou, X. Xu, Z. Tang and Z. Bo, *Adv. Energy Mater.*, 2021, **11**, 2102591.

27 L. Ma, S. Zhang, J. Zhu, J. Wang, J. Ren, J. Zhang and J. Hou, *Nat. Commun.*, 2021, **12**, 5093.

28 D.-L. Ma, Q.-Q. Zhang and C.-Z. Li, *Angew. Chem., Int. Ed.*, 2023, **62**, e202214931.

29 A. Bondi, *J. Phys. Chem.*, 1964, **68**, 441–451.

30 W. Zhu, A. P. Spencer, S. Mukherjee, J. M. Alzola, V. K. Sangwan, S. H. Amsterdam, S. M. Swick, L. O. Jones, M. C. Heiber, A. A. Herzing, G. Li, C. L. Stern, D. M. DeLongchamp, K. L. Kohlstedt, M. C. Hersam, G. C. Schatz, M. R. Wasielewski, L. X. Chen, A. Facchetti and T. J. Marks, *JACS*, 2020, **142**, 14532–14547.

31 P. W. M. Blom, V. D. Mihailetchi, L. J. A. Koster and D. E. Markov, *Adv. Mater.*, 2007, **19**, 1551–1566.

32 M. Stolterfoht, S. Shoaee, A. Armin, H. Jin, I. Kassal, W. Jiang, P. Burn and P. Meredith, *Adv. Energy Mater.*, 2017, **7**, 1601379.

33 Q. Liao, Q. Kang, Y. Yang, C. An, B. Xu and J. Hou, *Adv. Mater.*, 2020, **32**, 1906557.

34 J. Liu, S. Chen, D. Qian, B. Gautam, G. Yang, J. Zhao, J. Bergqvist, F. Zhang, W. Ma, H. Ade, O. Inganäs, K. Gundogdu, F. Gao and H. Yan, *Nat. Energy*, 2016, **1**, 16089.

35 P. K. Nayak, S. Mahesh, H. J. Snaith and D. Cahen, *Nat. Rev. Mater.*, 2019, **4**, 269–285.

36 X. Cheng, M. Li, Z. Guo, J. Yu, G. Lu, L. Bu, L. Ye, H. Ade, Y. Chen and Y. Geng, *J. Mater. Chem. A*, 2019, **7**, 23008–23018.

37 L. Ye, K. Weng, J. Xu, X. Du, S. Chandrabose, K. Chen, J. Zhou, G. Han, S. Tan, Z. Xie, Y. Yi, N. Li, F. Liu, J. M. Hodgkiss, C. J. Brabec and Y. Sun, *Nat. Commun.*, 2020, **11**, 6005.